A designed wall roughness approach to improve turbulent heat transfer to supercritical CO_2 flowing in horizontal tubes

Wang, Jianyong; Yang, Jun; Gong, Jishuang; Zhao, Chunrong; Hooman, Kamel

DOI
10.1016/j.supflu.2022.105738

Publication date
2022

Document Version
Final published version

Published in
Journal of Supercritical Fluids

The Journal of Supercritical Fluids 190 (2022) 105738

Contents lists available at ScienceDirect

The Journal of Supercritical Fluids

journal homepage: www.elsevier.com/locate/supflu

A designed wall roughness approach to improve turbulent heat transfer to supercritical CO_2 flowing in horizontal tubes

Jianyong Wang [a,b,*], Jun Yang [b], Jishuang Gong [b], Chunrong Zhao [c], Kamel Hooman [d]

[a] School of Aeronautics and Astronautics, Shenzhen Campus of Sun Yat-sen University, Shenzhen, Guangdong 518107, PR China
[b] School of Aeronautics and Astronautics, Sun Yat-sen University, Guangzhou, Guangdong 510275, PR China
[c] School of Aerospace, Mechanical and Mechatronic Engineering, The University of Sydney, Darlington, NSW 2006, Australia
[d] Department of Process and Energy, Delft University of Technology, Leeghwaterstraat 39, 2628 CB Delft, the Netherlands

HIGHLIGHTS

- Uniform sand-grain roughness greatly improves horizontal supercritical heat transfer.
- Regional wall roughness approach has been designed.
- Partial wall roughness significantly reduces the extra flow resistance.
- Influences of roughness height were discussed in detail.

GRAPHICAL ABSTRACT

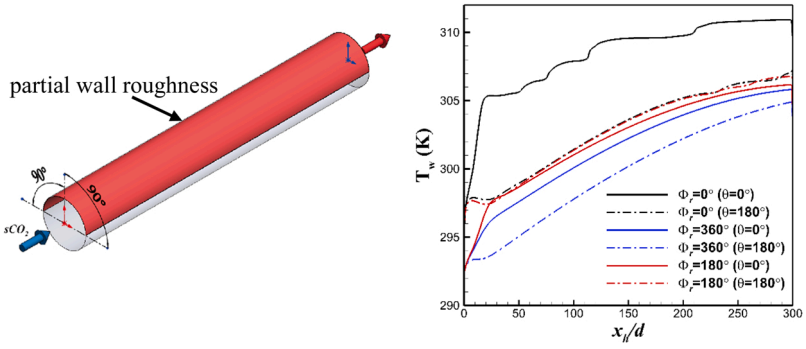

ARTICLE INFO

Keywords:
Supercritical flow
Horizontal pipe
Sand-grain roughness
Partly
Uniform heat transfer

ABSTRACT

Supercritical flow through a horizontal pipe leads to a non-uniform peripheral wall temperature distribution even when the wall heat flux is kept constant and uniform. This is attributed to lower heat transfer coefficient at the top section where the denser fluid tends to sink. Hence, to obtain a uniform wall temperature, a designed wall roughness is devised. Uniform sand-grain roughness is employed to only partly cover the top half of the pipe wall. Numerical simulations were conducted using the SST $k-\omega$ turbulence model. The simulation results indicate that our proposed design can lead to a more uniform heat transfer distribution over the wall periphery compared with the smooth pipe. An extreme case was also considered where the inner wall was completely covered with roughness elements. While heat transfer augmentation was observed for this case, the excess pressure drop was prohibitively higher compared with a pipe with designed wall roughness.

Abbreviations: CFD, computational fluid dynamics; CST, concentrating solar thermal; DNS, direct numerical simulations; EDM, electrical discharge machining; NIST, National Institute of Standards and Technology; N-S, Navier-Stokes; PWR, pressurized water reactor; QUICK, Quadratic Upstream Interpolation for Convective Kinematics; RANS, Reynolds-Averaged Navier-Stokes; sCO_2, supercritical carbon dioxide; SIMPLEC, Semi-Implicit Method for Pressure Linked Equations-Consistent; SST, shear-stress transport.

* Corresponding author at: School of Aeronautics and Astronautics, Shenzhen Campus of Sun Yat-sen University, Shenzhen, Guangdong 518107, PR China.
E-mail address: wangjiany5@mail.sysu.edu.cn (J. Wang).

https://doi.org/10.1016/j.supflu.2022.105738
Received 22 May 2022; Received in revised form 5 September 2022; Accepted 5 September 2022
Available online 8 September 2022

Nomenclature

Latin symbols

a_1	Constant in the μ_t expression of the shear stress transport model
C_S	Roughness constant
c_P	Specific heat at constant pressure [J/kg K]
d	Diameter [m]
D_ω, D_ω^+	Cross diffusion term [W/m^3]
f	Friction factor
F_1, F_2	Blending function
g	Acceleration due to gravity [m/s^2]
G	Mass flux [kg/m^2 s]
G_k, $\widetilde{G}_k$, G_ω	Production term in the turbulence transport equations [W/m^3]
h	Heat transfer coefficient [W/m^2 K]
H	Total enthalpy [J/kg]
k	Turbulence kinetic energy [m^2/s^2]
K_S	Roughness height [m]
P	Pressure [Pa]
q	Heat flux [W/m^2]
U	Component of the velocity vector [m/s]
Re	Reynolds number
S	Strain rate magnitude [1/s]
T	Temperature [K]
x, y, z	Distance in Cartesian coordinates [m]
$y+$	Dimensionless distance from wall
Y_k, Y_ω	Dissipation term in the turbulence transport equations [W/m^3]

Greek symbols

α^*	Coefficient to damp the turbulent viscosity
α_0^*, α_∞^*, α_∞, $\alpha_{\infty,1}$, $\alpha_{\infty,2}$	Model constant
β_i, β_∞^*, $\beta_{i,1}$, $\beta_{i,2}$	Model constant
Γ_k, Γ_ω	Effective diffusivity of k and ω [kg/m s]
Φ_r	Central angle for the roughness area [°]
Φ_1, Φ_2	Auxiliary variable in the blending functions
λ	Thermal conductivity [W/m K]
μ	Dynamic viscosity [kg/m s]
μ_t	Turbulent eddy viscosity [kg/m s]
θ	Circumferential direction in cylindrical coordinates [°]
ρ	Density [kg/m^3]
σ_k, σ_ω	Turbulent Prandtl number for k and ω of the shear stress transport model
$\sigma_{k,1}$, $\sigma_{k,2}$	Turbulent Prandtl number for k of the Wilcox $k-\omega$ and standard $k-\varepsilon$ model
$\sigma_{\omega,1}$, $\sigma_{\omega,2}$	Turbulent Prandtl number for ω of the Wilcox $k-\omega$ and ω-transformed standard $k-\varepsilon$ model
ω	Specific dissipation rate [1/s]
Δ	Absolute roughness height [m]

Subscripts

cr	Critical
h	Heated section
in	Inlet
m	Mean
o	Overall
out	Outlet
pc	Pseudo-critical
r	Rough
t	Top
w	Wall

1. Introduction

Supercritical carbon dioxide, (sCO_2), has been suggested as working fluids for power cycles embedded in the next-generation concentrating solar thermal (CST) plants [1,2] and also as coolant for nuclear reactors [3,4] or in the refrigeration industry [5,6].

The assumption of constant thermosphysical properties do not hold for sCO_2 as it experiences significant property variation in the vicinity of the pseudocritical temperature T_{pc} [6]. The effects of these property variations on turbulent heat transfer to sCO_2 flow through vertical pipes have been investigated in the 1960 s [7–12]. Those pioneering studies were followed by contemporary experiments relying on advanced measurement techniques [13–15]. It is well-documented that buoyant forces, induced by density variation, affect vertical turbulent supercritical heat transfer through two mechanisms, namely, the "direct" one through the structural turbulence production by buoyancy and the more dominant "indirect" one through the distortion of the velocity profiles that further vary the turbulence kinetic energy distribution.

Heat transfer to turbulent sCO_2 flow through horizontal pipes has also gained attention [16–19]. Different from the vertical cases, where the buoyant force is parallel to the mainstream, in horizontal pipes the buoyant force is perpendicular to the mainstream; therefore, the secondary flow would affect the heat transfer in a different way. The sCO_2 heating experiments by Adebiyi and Hall in early 1970s [20] reported that buoyancy leads to the salient heterogeneity of heat transfer over the circumference where the temperatures along the top wall are much higher than those along the bottom wall, indicting serious heat transfer deterioration in the top region. Computational fluid dynamics (CFD) simulations, direct numerical simulations (DNS) and Reynolds-Averaged Navier-Stokes (RANS) modeling [21–24], demonstrated that this impairment is attributed to buoyancy-induced secondary flows taking the accumulated lighter and hotter sCO_2 fluids to the top wall. Wang et al. [25] investigated the effect of tube diameter (4.6–22 mm) on turbulent heat transfer to sCO_2 flowing in horizontal tubes and concluded that the overall heat transfer performance was negatively influenced by the strong buoyancy induced by property variation even for pipes of small diameter. In view of the above, the asymmetric tube wall temperature distribution, observed by experimental and numerical papers, can lead to thermal stress and fatigue affecting the tube longevity and structural integrity thereby presenting a safety concern and increasing the operation and maintenance cost in the long run.

Attempts were made to improve the turbulent heat transfer to supercritical flows though vertical pipes. For instance, wire matrix inserts [26] and internal helical-rib roughness [27–29] were suggested in the literature. He and co-workers [30,31] used both experimental and numerical techniques to study turbulent sCO_2 heat transfer characteristics in horizontal tubes filled with metal foams. It was reported that while the filled metal foams remarkably enhance the sCO_2 heat transfer and result in a more uniform wall temperature along the tube circumference, the flow resistance increased by 50–100%, leading to significant excess pressure drops. Li et al. [32] introduced internal helical-ribs to improve the supercritical heat transfer in horizontal pipes to note an improved heat transfer along the top wall thereby reducing the temperature difference over the circumference albeit at the expense of 20–100% extra pressure drop. To optimize a heat exchanger design the interplay between heat transfer coefficient and pressure drop has to be carefully investigated especially for sCO_2 tubes with large diameters [33].

In view of the above, this paper offers a designed roughness approach where roughness is induced only where the local heat transfer coefficient is to be increased. In particular uniform sand-grain roughness is

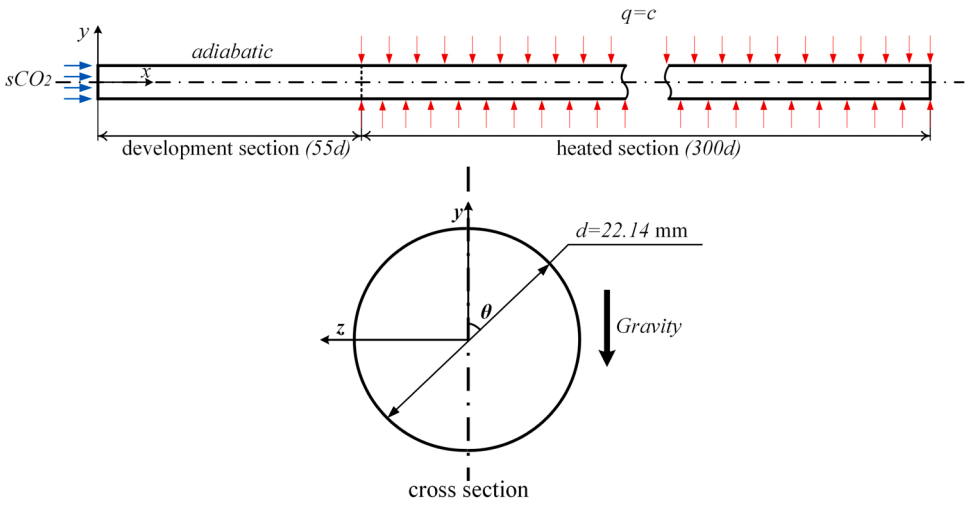

Fig. 1. Sketch of computational model.

proposed here to improve the turbulent heat transfer to horizontal sCO_2 pipes. Despite the fact that heat transfer augmentation though wall roughness was extensively studied in the literature [34–36], this technique has barely been employed in the supercritical heat transfer literature [37]. Additionally, for an effective thermal management with minimal excess pressure drop, the idea of regionally roughened walls is innovatively proposed in this work. CFD simulations based on RANS modeling have been conducted to shed light on the sCO_2 fluid flow and heat transfer within a horizontal tube with (partly) roughened wall. The influences of the roughness distribution and roughness heights on the heat transfer and pressure drop are investigated.

2. Numerical approach

2.1. Governing equations

Combining the advantages of the $k-\omega$ model and $k-\varepsilon$ model, the two-equation eddy viscosity model of SST (shear-stress transport) $k-\omega$ is able to properly resolve both the near-wall boundary region and the free stream area. Hence, the SST $k-\omega$ model is employed in this work to simulate the turbulent sCO_2 heat and fluid flow in a horizontal tube. The governing equations for the steady state flow are as follows:

Continuity:

$$\frac{\partial}{\partial x_i}(\rho u_i) = 0 \tag{1}$$

Momentum:

$$\frac{\partial}{\partial x_j}\left(\rho u_i u_j\right) = -\frac{\partial P}{\partial x_i} + \rho g_i + \frac{\partial}{\partial x_j}\left[\mu\left(\frac{\partial u_i}{\partial x_j} + \frac{\partial u_j}{\partial x_i}\right)\right] + \frac{\partial}{\partial x_j}\left(-\rho\overline{u_i' u_j'}\right) \tag{2}$$

Energy:

$$\frac{\partial}{\partial x_i}(\rho u_i H) = \frac{\partial}{\partial x_i}\left(\lambda\frac{\partial T}{\partial x_i} - \rho\overline{u_i' h}\right) + \mu\Phi - \frac{\partial u_i}{\partial x_j}\left(\rho\overline{u_i' u_j'}\right) \tag{3}$$

where the energy dissipation term Φ is defined as:

$$\Phi = \left(\frac{\partial u_i}{\partial x_j} + \frac{\partial u_j}{\partial x_i}\right)\frac{\partial u_i}{\partial x_j} \tag{4}$$

λ denotes the thermal conductivity and the additional terms of $\rho\overline{u_i' h}$, $\rho\overline{u_i' u_j'}$ are due to the turbulent fluxes.

The transport equations for the turbulence are expressed as below:

$$\frac{\partial}{\partial x_i}(\rho k u_i) = \frac{\partial}{\partial x_j}\left(\Gamma_k\frac{\partial k}{\partial x_j}\right) + \widetilde{G_k} - Y_k + S_k \tag{5}$$

$$\frac{\partial}{\partial x_i}(\rho k\omega u_i) = \frac{\partial}{\partial x_j}\left(\Gamma_\omega\frac{\partial \omega}{\partial x_j}\right) + G_\omega - Y_\omega + D_\omega + S_\omega \tag{6}$$

where the production of the turbulence kinetic energy due to mean velocity gradient $\widetilde{G_k}$ is calculated as:

$$\widetilde{G_k} = min(G_k, \quad 10\rho\beta^* k\omega) \tag{7}$$

and $G_k = -\rho\overline{u_i' u_j'}\left(\partial u_j/\partial x_i\right)$.

The generation of specific dissipation rate, ω is computed as:

$$G_\omega = \frac{\alpha}{\nu_t}G_k \tag{8}$$

$$\alpha = \frac{\alpha_\infty}{\alpha^*}\left[\frac{\alpha_0 + Re_t/R_\omega}{1 + Re_t/R_\omega}\right] \tag{9}$$

where R_ω is a constant and the α^* is introduced to damp the turbulent viscosity leading to a low-Reynolds number correction.

$$\alpha^* = \alpha_\infty^*\left(\frac{\alpha_0^* + Re_t/R_k}{1 + Re_t/R_k}\right) \tag{10}$$

in which $\alpha_0^* = \beta_i/3$, $Re_t = \rho k/\mu\omega$, and $\alpha^* = \alpha_\infty^* = 1$ is set for the case of high Reynolds numbers.

$$\alpha_\infty = F_1\alpha_{\infty,1} + (1 - F_1)\alpha_{\infty,2} \tag{11}$$

where $\alpha_{\infty,1} = \beta_{i,1}/\beta_\infty^* - k^2/\sigma_{\omega,1}\sqrt{\beta_\infty^*}$ and $\alpha_{\infty,2} = \beta_{i,2}/\beta_\infty^* - k^2/\sigma_{\omega,2}\sqrt{\beta_\infty^*}$.

The effective diffusivity (Γ) for the turbulence equations of k and ω are defined as:

$$\Gamma_k = \mu + \frac{\mu_t}{\sigma_k} \tag{12}$$

$$\Gamma_\omega = \mu + \frac{\mu_t}{\sigma_\omega} \tag{13}$$

where μ_t represents the turbulent viscosity

$$\mu_t = \frac{\rho k}{\omega}\frac{1}{max\left[\frac{1}{\alpha^*}, \frac{SF_2}{a_1\omega}\right]} \tag{14}$$

here S denotes the strain rate magnitude. The turbulent Prandtl numbers σ_k, σ_ω are calculated as:

$$\sigma_k = \frac{1}{\frac{F_1}{\sigma_{k,1}} + \frac{1-F_1}{\sigma_{k,2}}} \tag{15}$$

Table 1
Details of validation calculation cases from tests by Adebiyi and Hall [20].

Cases	$\dot{m}$ (kg/s)	T_{in} (℃)	q (kW/m^2)	P (MPa)	T_{out} (℃)	$\mathbf{Re}_{in}$
1	0.148	15.4	15.1	7.59	21.3	103,464
2	0.0773	14.2	5.2	7.603	18.4	52,710

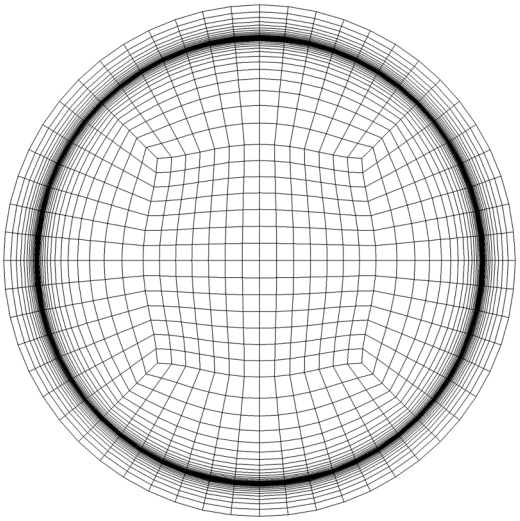

Fig. 2. Grids used for validations against experiments by Adebiyi and Hall [20].

$$\sigma_\omega = \frac{1}{\frac{F_1}{\sigma_{\omega,1}} + \frac{1-F_1}{\sigma_{\omega,2}}} \tag{16}$$

F_1, F_2 are the blending functions for the SST $k-\omega$ model:

$$F_1 = tanh\left(\Phi_1^4\right) \tag{17}$$

$$\Phi_1 = min\left[max\left(\frac{\sqrt{k}}{0.09\omega y}, \frac{500\mu}{\rho y^2 \omega}\right), \frac{4\rho k}{\sigma_{\omega,2} D_\omega^+ y^2}\right] \tag{18}$$

$$D_\omega^+ = max\left[2\rho \frac{1}{\sigma_{\omega,2}} \frac{1}{\omega} \frac{\partial k}{\partial x_j} \frac{\partial \omega}{\partial x_j}, 10^{-10}\right] \tag{19}$$

$$F_2 = tanh\left(\Phi_2^2\right) \tag{20}$$

$$\Phi_2 = max\left[2\frac{\sqrt{k}}{0.09\omega y}, \frac{500\mu}{\rho y^2 \omega}\right] \tag{21}$$

where D_ω^+ represents the positive portion of the cross diffusion term D_ω

$$D_\omega = 2(1-F_1)\rho\sigma_{\omega,2} \frac{1}{\omega} \frac{\partial k}{\partial x_j} \frac{\partial \omega}{\partial x_j} \tag{22}$$

The dissipation term for k and ω are:

$$Y_k = \rho\beta^* \omega \tag{23}$$

$$Y_\omega = \rho\beta_i \omega^2 \tag{24}$$

where $\beta_i = F_1\beta_{i,1} + (1-F_1)\beta_{i,2}$.

S_k, S_ω are the source terms that are set to zero in this work; all other model constants are set the same as those in [38].

2.2. Physical model and numerical strategies

Fig. 1 displays the computational model used in the present study. The tube diameter is set as $d = 22.14$ mm similar to Adebiyi and Hall's experimental test set up [20] where significant heat transfer non-uniformity over the pipe circumference was reported along with serious top and bottom wall temperature mismatch. As shown, a preceding development section with length of 1.22 m ($\approx 55\ d$) is added to ensure fully developed turbulent sCO_2 flows before it reaches the heated region with tube length of 6.642 m ($= 300\ d$). Here, θ is the circumferential angle and $\theta = 0°$, $\theta = 180°$ represents the top and bottom tube wall, respectively. The entire computational model shown here is simulated using hexahedral mesh with 3.6×10^6 grids.

The velocity and pressure terms are coupled using the Semi-Implicit Method for Pressure Linked Equations-Consistent (SIMPLEC) algorithm. The "body force weighted" scheme is employed to discretise the pressure term and the Quadratic Upstream Interpolation for Convective Kinematics (QUICK) scheme is used for the energy and momentum equations. The first order accuracy is selected to march the turbulence transport equations for better convergence, which has been verified to have negligible effects on the results. The real-gas properties needed for sCO_2 computations are updated based on the generated look-up table from the solver incorporated National Institute of Standards and Technology (NIST) database. The mass flow inlet and pressure outlet boundaries are applied while the wall is modeled as adiabatic in the developing region and constant heat flux has been imposed to the heating wall. For the rough wall, two parameters, namely, the roughness height (K_s) and the roughness constant (C_s) are specified, where $C_s = 0.5$ is set for the uniform sand-grain roughness.

When using the low-Reynolds number model of SST $k-\omega$ model, fine mesh (non-dimensional wall distance $y^+ \approx 1.0$) is required to directly solve the governing equations all the way to the wall. In order to properly resolve the sCO_2 flow and heat transfer behaviors in the near-wall region with significant property gradients, quite fine mesh ($y^+ < 0.5$) has been implemented. To ensure grid independence, we have doubled the total grid number to realize that the wall temperature variation is less than 1.5%. Also, the grids have been clustered near the starting of the heating section to better capture the details in the thermal entry region with sharp temperature gradient.

2.3. Model validations

2.3.1. Smooth tubes

This section demonstrates the reliability of the CFD results. In the absence of results pertinent to rough walls, the experimental ones reported by Adebiyi and Hall [20] on sCO_2 heat transfer heated in horizontal pipes with smooth walls (the diameter is the same as that employed in this work) are used for validation purpose. Two different conditions have been simulated, with details specified in Table 1. For a more rigorous examination on the deterioration, the tube wall is included in the computations, as shown in Fig. 2 for the used grids. Fig. 3 compares the simulation results against those of measurements. As seen, the buoyancy generates a significant temperature difference between the two surfaces, the temperatures are higher along the top wall, indicating lower local heat transfer there. The temperature non-uniformity has been well reproduced here with good consistency exhibited for the bottom wall, the maximum deviation for the top wall temperatures is 14.7% compared with experimental data reported in [20] and the inconsistency for the outlet bulk temperature is less than 0.5%.

2.3.2. Rough tubes

Recent experimental measurements by Tikadar et al. [39] are used to validate the SST $k-\omega$ model on reproducing the flow and heat transfer for flow through rough pipes. In their tests, the heat transfer and pressure drop in the Inconel-Nickel fuel rod for pressurized water reactor (PWR) have been measured, where the Inconel fuel rod was modified with three-dimensional (Diamond-shaped blocks) surface roughness; more details can be found in [39]. Fig. 4(a) compares the calculated Darcy friction factors of the smooth Nickel domain and the rough

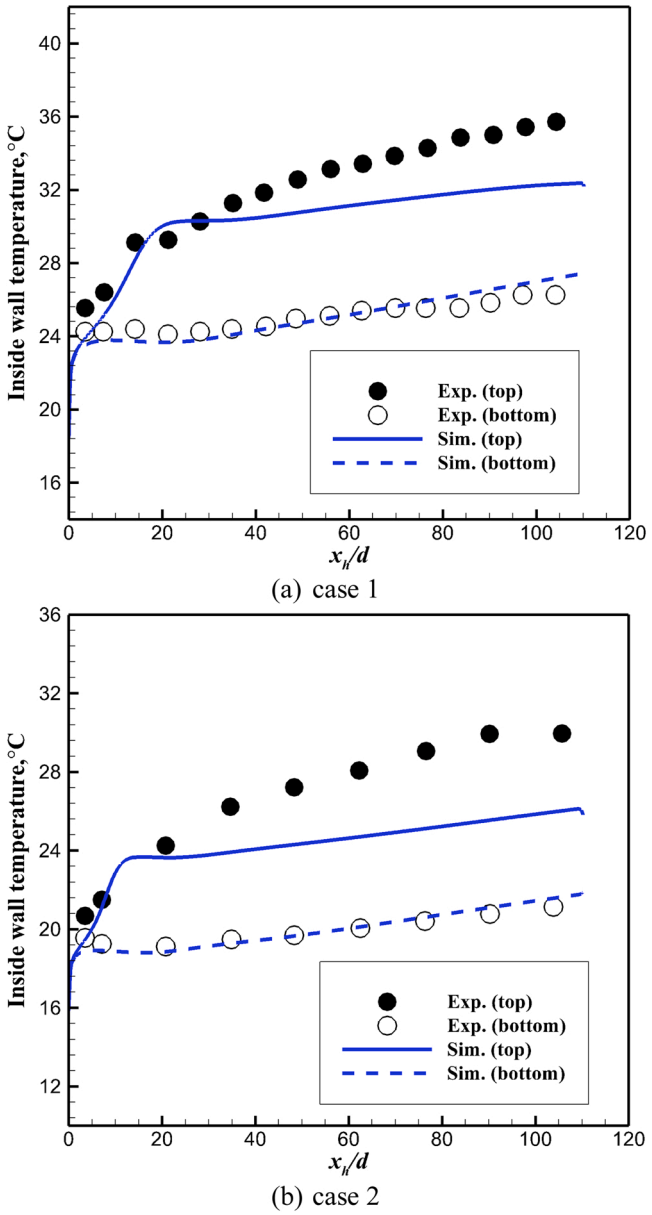

Fig. 3. Wall temperature distributions simulated using SST $k-\omega$ turbulence model compared against experimental measurements by Adebiyi and Hall [20] (subscript 'h' in 'x_h' represents 'heating').

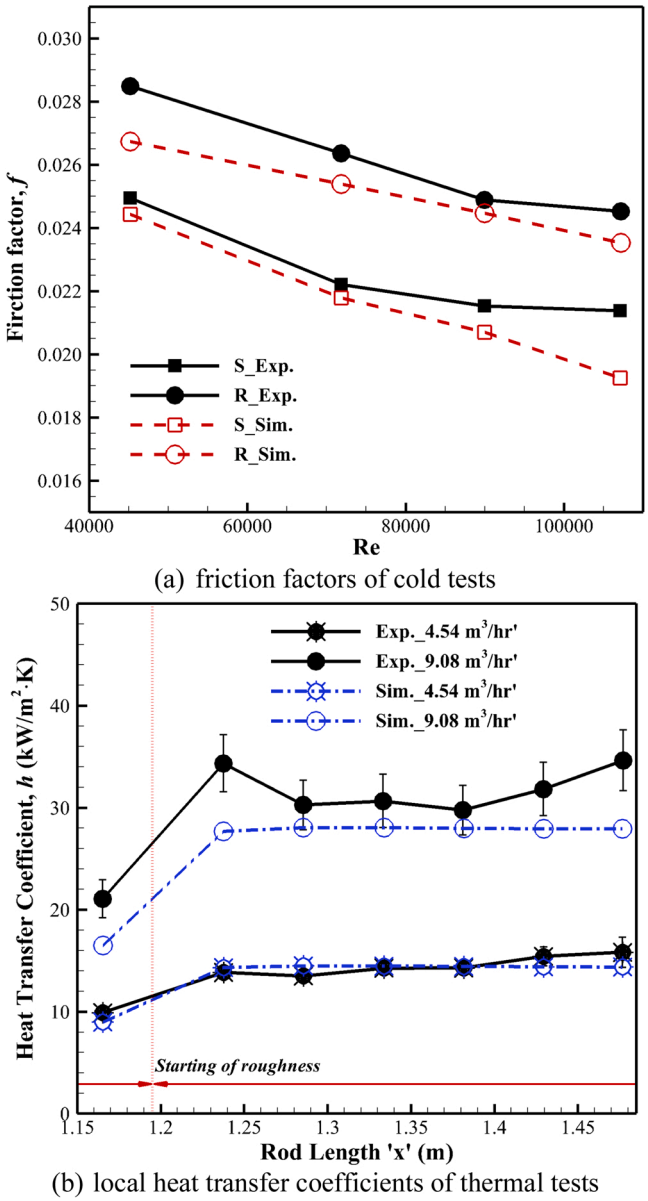

Fig. 4. Rough pipe flow simulated using SST $k-\omega$ turbulence model compared against experimental measurements by Tikadar et al. [39].

Inconel part against the experimental measurements, where four cold tests with the Reynolds number **Re** ranging from 45,145 to 107,096 have been performed (details are specified in Table 2). One notes a very good agreement between our predictions and the experimental data reported therein. The largest deviation for the smooth test is less than 10%. Fig. 4(b) displays the local heat transfer coefficient distributions along the entire Inconel rod (including the beginning smooth section) of two thermal tests, where the Inconel rod was heated and the volumetric flow rate changes from 4.54 m^3/h to 9.08 m^3/h, as illustrated in Table 3. As observed, the heat transfer enhancement caused by the roughness has been well reproduced by the simulations, and a very good agreement is noted for the case of low mass flow rate. However, with higher mass flow rate, the discrepancy grows and the heat transfer coefficients are underestimated, especially at the beginning and towards the end of the rough region. The error, nonetheless, is less than 19.5%. This can be attributed to the fact that the treatment of sand-grain roughness in the computation might weaken the vortex generations by the actual

Table 2
Details of validation cases from cold tests by Tikadar et al. [39].

Code	T_{in} (°C)	Pressure (MPa)	Flow rate (m^3/h)	**Re**
Test 1	31.88	0.404	5.04	45,145
Test 2	31.88	0.404	8.03	71,813
Test 3	31.88	0.404	10.06	89,991
Test 4	31.88	0.404	14.02	107,096

Table 3
Details of validation calculation cases from thermal tests by Tikadar et al. [39].

Code	T_{in} (°C)	Heat flux (kW/m^2)	Pressure (MPa)	Flow rate (m^3/h)	**Re**
Test 1	70	181	0.46	4.54	82,000
Test 2	70	181	0.46	9.08	166,000

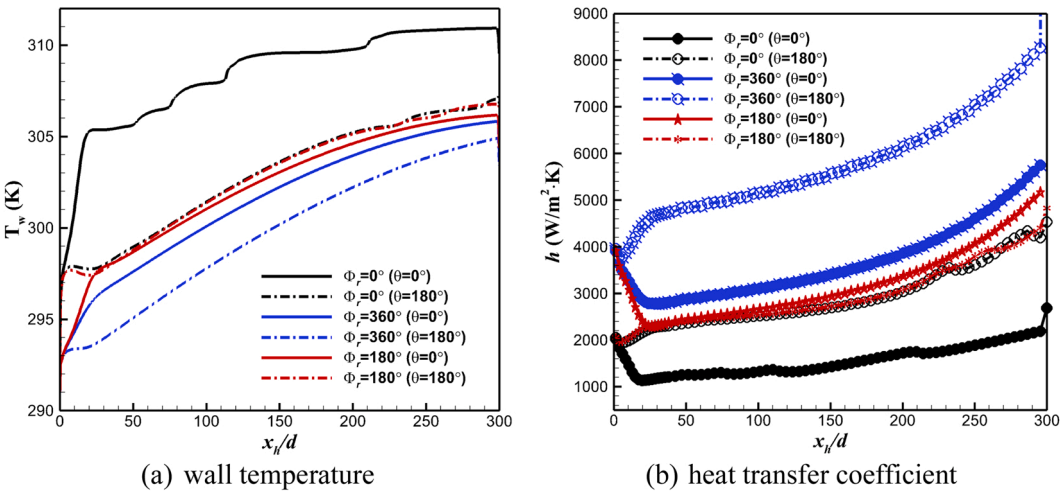

(a) wall temperature (b) heat transfer coefficient

Fig. 5. Heat transfer characteristics of turbulent sCO_2 flows along top and bottom wall in smooth, fully-roughened and half-roughened horizontal pipes under the condition of $P = 7.59$ MPa, $T_{in} = 15℃$, $G = 400$ kg/m^2 s and $q = 18$ kW/m^2 (Φ_r denotes central angle of wall roughness area).

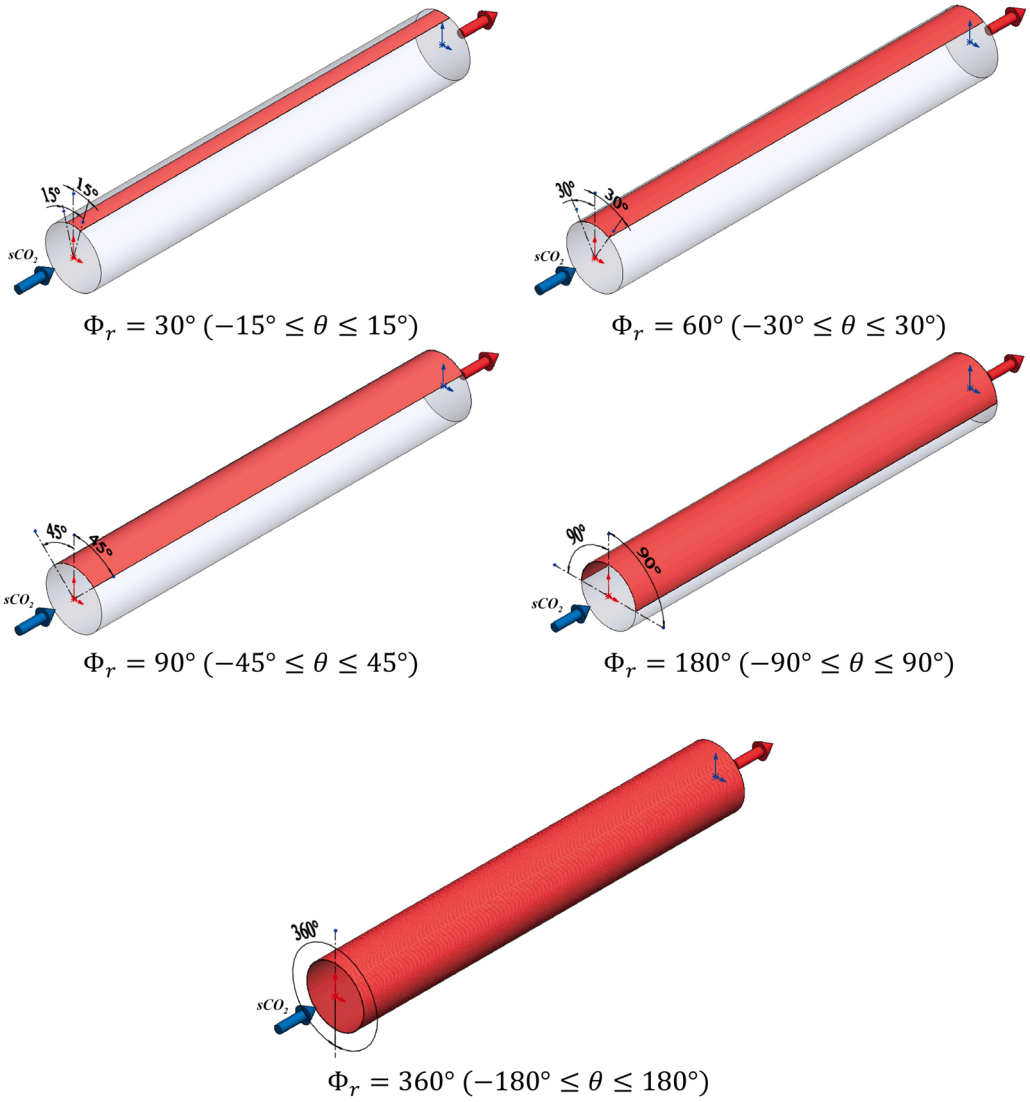

$\Phi_r = 30° (-15° \le \theta \le 15°)$ $\Phi_r = 60° (-30° \le \theta \le 30°)$

$\Phi_r = 90° (-45° \le \theta \le 45°)$ $\Phi_r = 180° (-90° \le \theta \le 90°)$

$\Phi_r = 360° (-180° \le \theta \le 180°)$

Fig. 6. Schematic of roughen heating walls for horizontal sCO_2 flows.

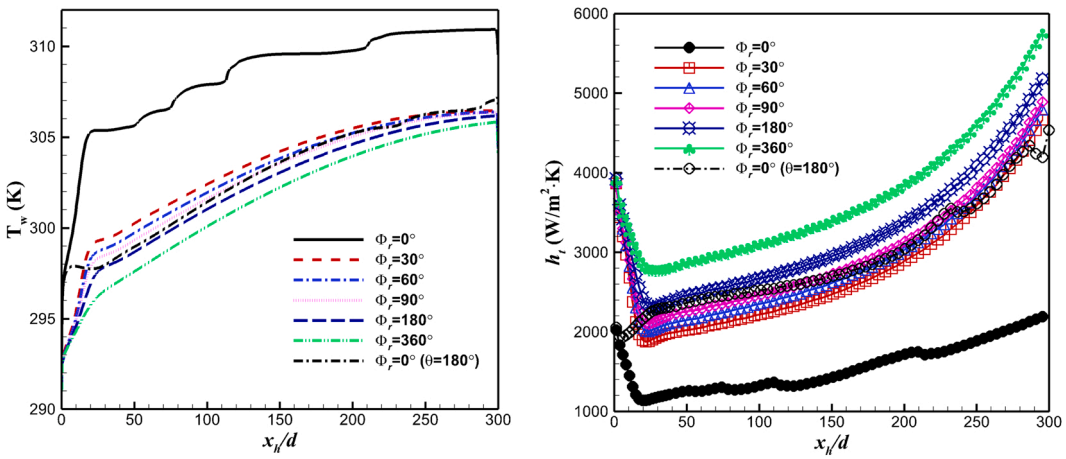

(a) wall temperatures (b) heat transfer coefficients

Fig. 7. Heat transfer characteristics of turbulent sCO_2 flows along top wall in smooth and various rough horizontal tubes, with distributions along bottom wall of smooth flows added as a representative (Φ_r denotes central angle of wall roughness area, subscript 't' in 'h_t' is abbreviation for 'top').

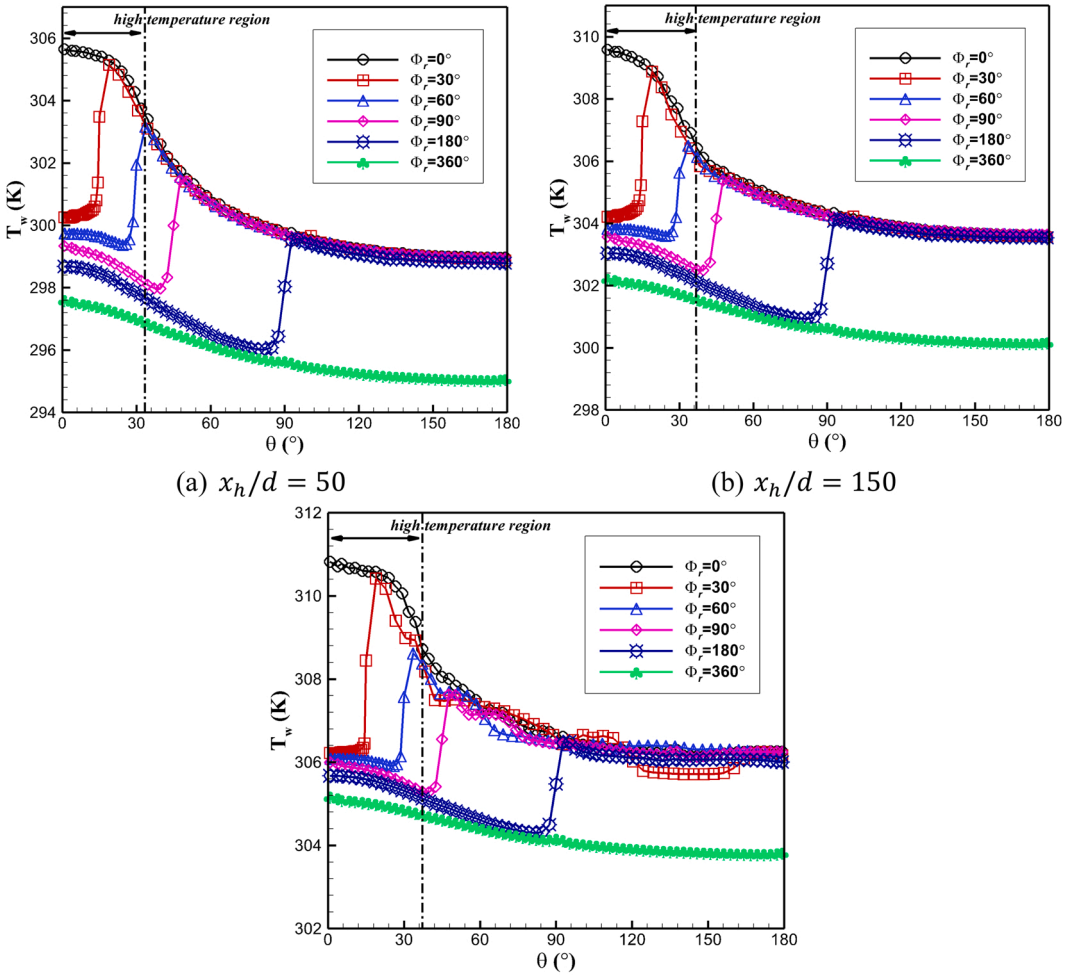

(a) $x_h/d = 50$ (b) $x_h/d = 150$

(c) $x_h/d = 250$

Fig. 8. Circumferential wall temperature distributions from top ($\theta = 0°$) to bottom ($\theta = 180°$) at different axial positions of smooth and various rough horizontal tubes (Φ_r denotes central angle of wall roughness area).

diamond-shaped blocks in the two particular regions. This is expected to be more pronounced at higher Reynolds numbers while the intermediate rough section shows a much better agreement.

These two sets of validations demonstrate that the selected SST $k-\omega$ model can reliably reproduce data for both sCO_2 heat transfer in horizontal smooth tubes and the pressure drop and heat transfer

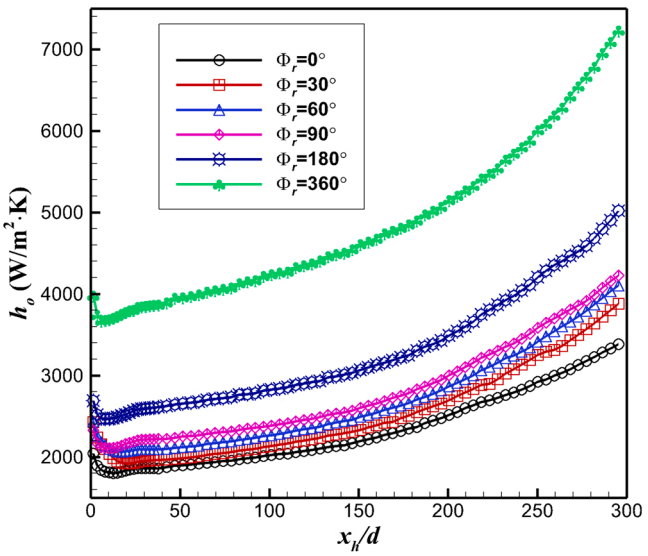

Fig. 9. Overall heat transfer coefficient distributions of turbulent sCO_2 flows along heating wall in smooth and various rough horizontal tubes (Φ_r denotes central angle of wall roughness area, subscript 'o' in 'h_o' represents 'overall').

characteristics of flow in pipes with rough walls. In addition, in the open literature, the SST $k-\omega$ model was commonly employed for the sCO_2 heat transfer simulations [40–43], including the most recent work by Li et al. [28,29,44] on the supercritical flow and heat transfer with internal helical-rib roughness where good accuracy was demonstrated. Therefore, this model has been used in this paper.

2.4. Proposition of the new idea of regional roughness

Turbulent sCO_2 heat and fluid flow in a smooth horizontal tube has been simulated where the inlet temperature $T_{in} = 15℃$, mass flux $G = 400\ \mathrm{kg/m^2\ s}$, heat flux $q = 18\ \mathrm{kW/m^2}$ and pressure $P = 7.59\ \mathrm{MPa}$, are used. The wall temperatures and heat transfer coefficients along the top and bottom pipe wall are plotted in Fig. 5 where the results pertinent to smooth walls are denoted by "$\Phi_r = 0°$". Similar to the distributions exhibited in Fig. 3, the temperature mismatch between the two peak surfaces are noted where higher temperature at the top wall are significantly different from lower values at the lower half of the pipe wall. In order to mitigate this, one needs to improve the heat transfer uniformity; here through using uniform sand-grain roughness at the pipe inner wall. According to the classical experiments by Nikuradse [45] on the pipe flows with sand-grain roughness, a moderate value of the relative roughness ($\overline{\Delta} = \Delta/d = 120$) is chosen leading to an absolute roughness height $\Delta = 0.1845\ \mathrm{mm}$. The simulation results for the fully rough tube under the same operating conditions are demonstrated in Fig. 5 with "$\Phi_r = 360°$". As seen, the top wall temperatures decline remarkably and heat transfer is augmented. However, since the bottom half of the wall is also roughened, the bottom wall temperatures also drop and the difference in the circumferential wall temperatures still exists, and the local heat transfer coefficients mismatch persists, as shown in Fig. 5(b). The variation in lower T_w is likely to cause greater differences in local heat transfer coefficient (over each cross-section) non-uniformity.

It is reasonable to roughen the top wall to increase the local heat transfer and bring it to a value close to that of the bottom smooth wall. The new idea of designed partial wall roughness is therefore examined. We initially roughen half of the tube wall with the sand-grain roughness in the top and the numerical outcomes are added to Fig. 5, denoted by

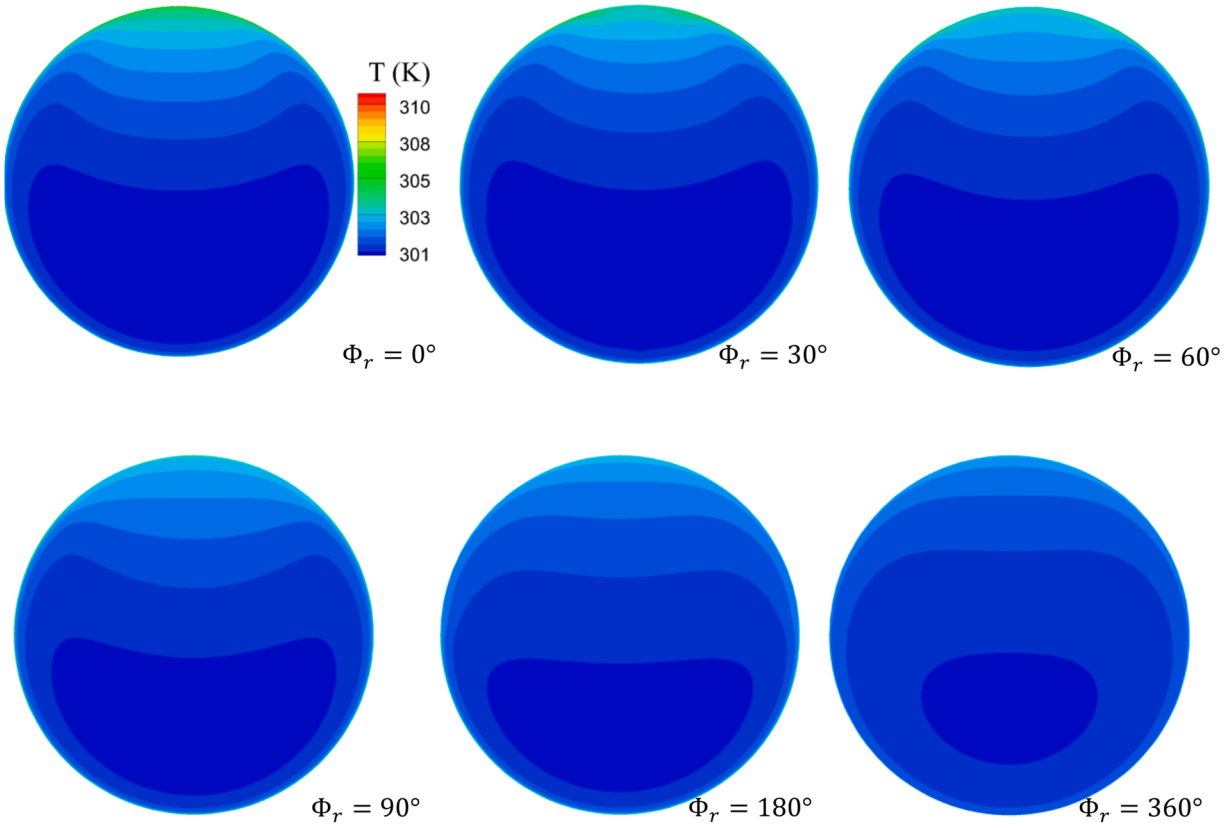

Fig. 10. Temperature contours of turbulent sCO_2 flows over cross section at $x_h/d = 250$ of smooth and various rough horizontal tubes (Φ_r denotes central angle of wall roughness area).

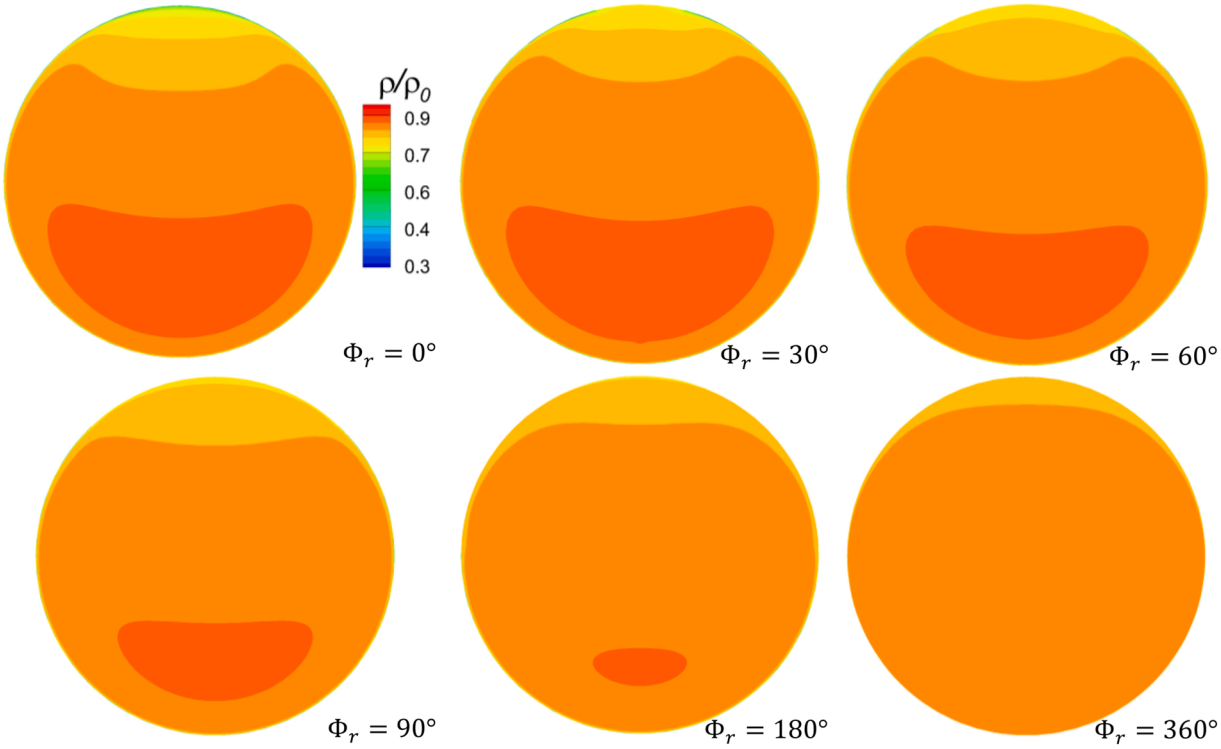

Fig. 11. Nondimensional density contours of turbulent sCO_2 flows over cross section at $x_h/d = 250$ of smooth and various rough horizontal tubes (Φ_r denotes central angle of wall roughness area, ρ_0 means sCO_2 fluid density at inlet).

"$\Phi_r = 180°$". As seen, the top wall temperature is now closer to that of the bottom wall. Here, a more uniform wall temperature and heat transfer coefficient (along the periphery) can be observed. In addition, as with a decrease in the roughness area, the flow resistance is likely to drop, we gradually shrink the roughness proportion to focus more on the very top wall region where the sCO_2 heat transfer deteriorates most. As illustrated in Fig. 6, besides the fully-rough and half-roughened approaches, three other cases of regional roughness distribution are investigated in this paper. Here, the central angle for the roughen part is represented by "Φ_r". Regarding the developments of these rough horizontal pipes in practice, the electrical discharge machining (EDM) can be employed, its feasibility has been verified in the manufacturing of the rough tubes for future heat transfer tests.

3. Results and discussion

3.1. Wall temperatures and heat transfer coefficients

Simulations on the turbulent sCO_2 fluid flow and heat transfer in the horizontal tube with different roughness designs have been conducted. Results pertinent to the smooth wall case have also been presented for comparison purpose. Beside the roughness distribution, all other parameters are kept the same as those in Section 2.4, with **Re** ranging from 1.07×10^5 to 1.66×10^5. The operating pressure is close to the critical point and the inlet temperature is set to be close to the liquid-like region where the drastic density variation is likely to cause significant buoyancy effects. The mass flux and heat load are typical values consistent with the practical use of supercritical heat exchangers and approach the conditions which have been validated in Section 2.3.1. Fig. 7 compares the sCO_2 heat transfer features along the top wall surface ($\theta = 0°$) for various cases where the deterioration usually occurs. Because the temperature distributions at the bottom wall ($\theta = 180°$) are quite similar for different cases except the entirely rough tube, as testified by Figs. 5(a) and 8, in the following discussion only the values along the bottom surface of the smooth pipe are added in Fig. 7 to illustrate the circumferential differences. As seen, with the development of thermal boundary layers, the wall temperatures increase and the heat transfer coefficient initially drops but then rapidly rises. Comparing the local distributions between the top and bottom walls of the smooth case, it can be noted that the entrance effects propagate further downstream over the top surface, which is due to the thicker boundary layer there. Fig. 7 (a) displays the top wall temperature distributions where all the rough wall cases can significantly reduce the top wall temperature and narrow the gap between the top and bottom wall temperatures. This is because the sCO_2 heat transfer near the top wall has been greatly improved as reflected in Fig. 7(b). This enhancement is more pronounced with the increasing roughness area. Compared to the fully-roughened tube, as shown in Fig. 5, the regionally-roughened cases perform better leading to more uniform heat transfer over the circumference.

The wall temperature distributions along the circumference over the cross section are presented in Fig. 8, where only half of the periphery is shown due to symmetry. Note that the fully-roughened case significantly reduces the wall temperatures over the whole pipe surface, but the circumferential difference persists even leading to higher heat transfer mismatch compared with the smooth case, as displayed in Fig. 5. For the partial roughness case, on the other hand, only the T_w values within the roughened top region decrease and the temperatures within the smooth section barely change. This leads to a more uniform distribution of both wall temperature and heat transfer coefficient. With the sCO_2 flowing downstream, the top wall temperature tends to be the same for various roughness designs considered here. Note that, for the smooth pipe, the higher temperature region around the top wall begins at the circumferential angle of $\theta \approx 28° - 37°$ (slightly expands downstream). This can be used to devise a more uniform wall temperature. One observes that

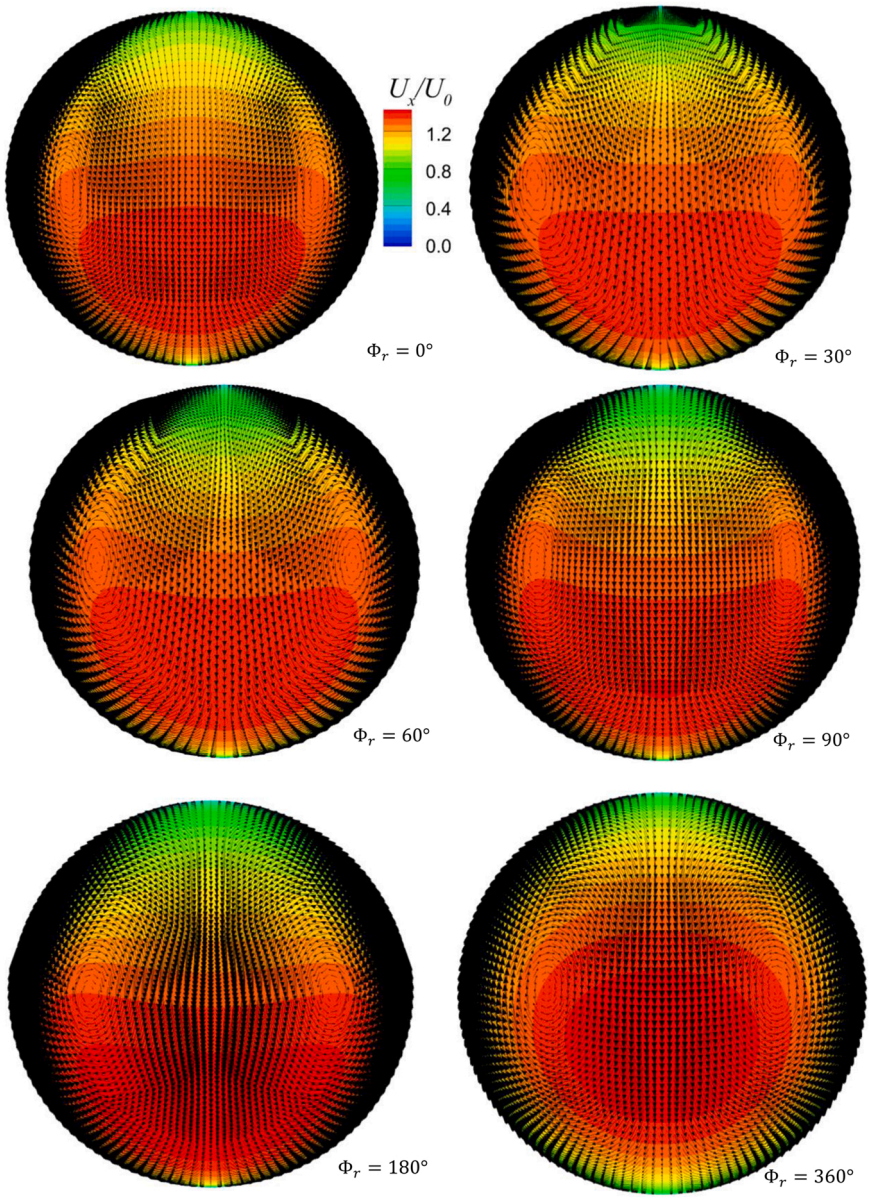

Fig. 12. Axial velocity contours and secondary vectors of turbulent sCO_2 flows over cross section at $x_h/d = 250$ of smooth and various rough horizontal tubes (Φ_r denotes central angle of wall roughness area, U_0 means sCO_2 fluid density at inlet).

among the studied cases, the partial roughness case with $\Phi_r = 60°(-30° \leq \theta \leq 30°)$ performs well at reducing the high top wall temperature, as shown in Fig. 8.

Fig. 9 presents the overall heat transfer coefficient h_o (averaged over each cross section) distribution along the wall. Compared to the smooth tube, roughening the pipe wall mitigates the heat transfer degradation in the top then improves the overall heat transfer performance of horizontal sCO_2 flows as well, and the improvement gets more pronounced as the roughness area expands and sCO_2 bulk temperature approaches the pseudocritical point where the buoyancy intensifies.

3.2. Flow field analysis

This section presents results for core flow or regions away from the wall. Figs. 10 and 11 show the temperature and density contours, respectively, over the entire cross section at $x_h/d = 250$ (far downstream in the developed region) for both smooth and rough cases. As seen, with the smooth tube ($\Phi_r = 0°$), buoyancy gives rise to a secondary flow (see Fig. 12), which then sweeps the near-wall sCO_2 fluids and rises upwards, and the lighter and hotter low-momentum sCO_2 fluids are accumulated near the top surface, thereby lowering the heat transfer there. With the roughness introduced, the high-temperature area with those low-density fluids gathered in the top half diminishes even vanishes. Increasing the roughness area, the sCO_2 heat transfer gets improved as one would expect.

Fig. 12 displays the contours of axial sCO_2 velocity, where the vectors over the yz plane have been added to the velocity contours. For the smooth wall case, due to the blocked secondary circulation caused by flow accumulation, a second velocity peak emerges near the top surface. Consequently, the velocity gradient reduces there leading to a more flattened velocity profile thereby the production of turbulence kinetic energy is affected, as depicted in Fig. 13. Fig. 14 indicates the radial

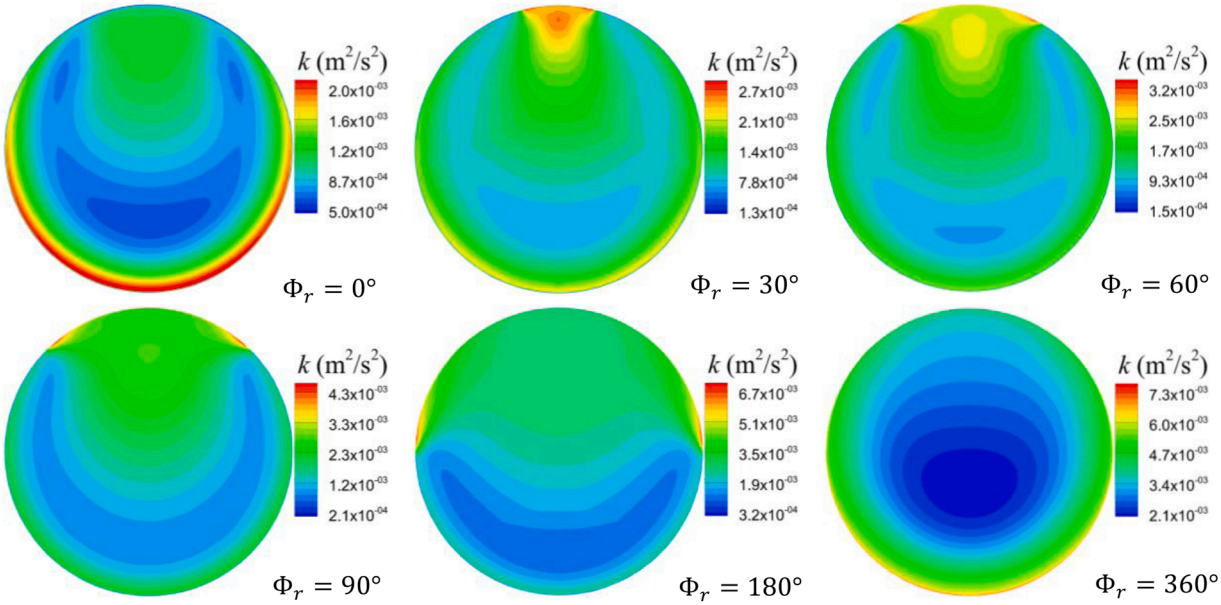

Fig. 13. Turbulence kinetic energy contours of sCO_2 flows over cross section at $x_h/d = 250$ of smooth and various rough horizontal tubes (Φ_r denotes central angle of wall roughness area).

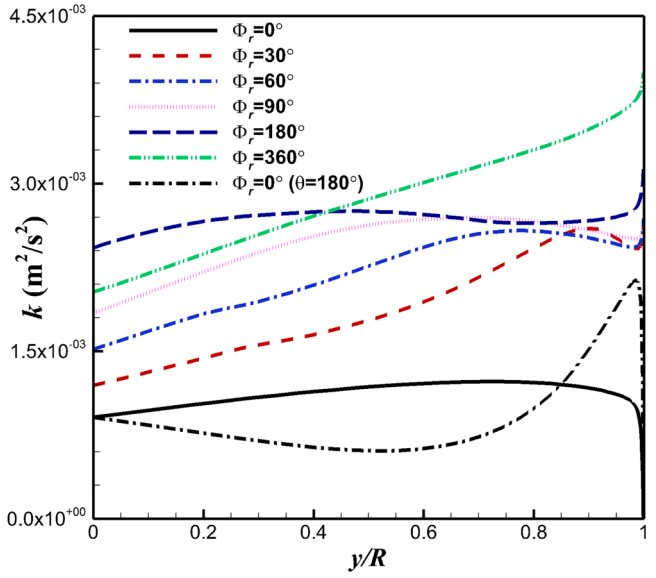

Fig. 14. Distributions of turbulence kinetic energy along radius at top wall ($\theta = 0°$) at $x_h/d = 250$ of smooth and various rough horizontal tubes, where variation at bottom wall ($\theta = 180°$) for smooth flows is added for comparison (Φ_r denotes central angle of wall roughness area).

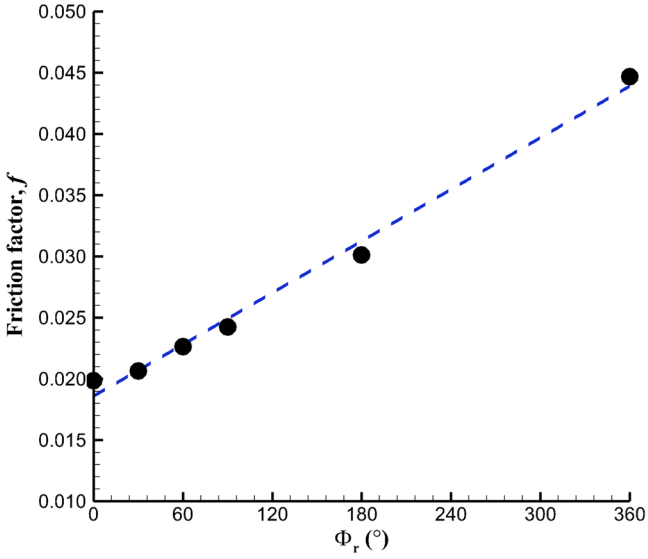

Fig. 15. Friction factor variations of turbulent sCO_2 flows in smooth and various rough horizontal pipes.

variation of turbulence kinetic energy (k) for smooth wall ($\Phi_r = 0°$), where k values close to the top wall are much lower than those near the bottom one. These lead to a heat transfer deterioration at the top wall. With introduction of the wall roughness, nonetheless, the thick boundary layer at the top wall is disturbed as one would expect. As seen in Fig. 12 for the roughness case of $\Phi_r = 30°$, the circulation is intensified close to the top wall. The anchor-shape velocity contour with a second peak disappears and a sharper velocity gradient at the top wall is observed which in turn will increase the shear stress and the turbulence kinetic energy production, as demonstrated in Fig. 13. As Fig. 14 demonstrates the k values are markedly higher in the top half for the rough cases, especially in the near-wall region. In addition, the introduced sand-grain wall roughness destroys the viscous sublayer and generates vortex itself, promoting the turbulence kinetic energy production as well. Both these two mechanisms enhance the heat transfer to sCO_2 flow. Roughening a bigger portion of the wall, the larger chunk of low-momentum flow is disturbed leading to enhancements presented in Fig. 9 for the entirely rough pipe. This can also be deduced based on the notably reduced secondary circulating activities of the near-wall fluid observed in Fig. 12 for the case of $\Phi_r = 360°$. However, similar to the smooth wall case, the evident difference in the turbulence kinetic energy distribution between the bottom and top wall is still there for the fully rough pipe, as shown in Fig. 13.

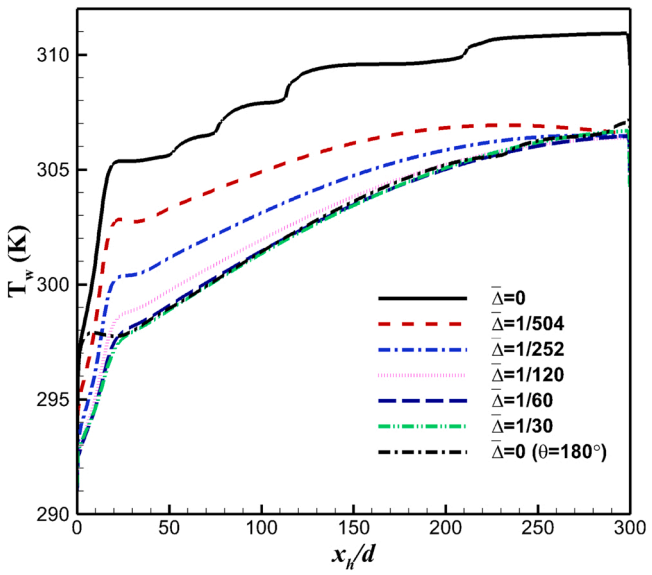

Fig. 16. Wall temperature distributions of horizontal sCO_2 flows along tube top wall with various roughness heights, where partial roughness scheme of $\Phi_r = 60^\circ$ is issued and variation at the bottom wall ($\theta = 180^\circ$) for smooth flows is added for comparison.

3.3. Frictional pressure drop

The frictional pressure drop is discussed here mainly because it is a crucial factor to be considered in heat exchanger design. As the roughness is added onto the pipe surface, more vortexes will be generated causing excess pressure drop. Fig. 15 displays the variations of the Darcy friction factor for the smooth and rough cases, computed as below:

$$f = \frac{-2(\frac{\Delta P}{\Delta x})d}{\rho_m U_m^2} \tag{25}$$

where the $\Delta P/\Delta x$ is the pressure drop per unit length, and the needed thermo-physical properties are evaluated at the mean temperature T_m, which is the arithmetic mean value of the inlet and outlet temperatures:

$$T_m = \frac{T_{in} + T_{out}}{2} \tag{26}$$

As seen, the introduced sand-grain roughness obviously increases the frictional pressure drop and the influence of the roughness proportions is prominent. For instance, as for the case of $\Phi_r = 30^\circ$ where the roughness targets more particularly on the top surface, the friction factor slightly rises (by around 4%) compared with that of the smooth tube. Whereas for the full roughness condition, the f value is more than doubled, increases by more than 125%. It is worth noting that the friction factor augments nearly linearly with Φ_r. This trend can be explained based on the fact that the angle Φ_r determines the roughness area with the linear formula $A_r = \Phi_r \pi r L/180$, while the friction loss is directly proportional to the roughness area.

3.4. Effect of roughness height

Based on the above analysis, considering both the heat transfer and pressure drop characteristics, the optimal regional roughness scheme $\Phi_r = 60^\circ$ under this investigated condition is chosen for a sensitivity analysis where the roughness height is changed while all other parameters are kept constant. Aligned with the classic tests by Nikuradse [45], five different roughness heights are studied, where the relative heights to the tube diameter are $\bar{\Delta} = \Delta/d = 1/504,\ 1/252,\ 1/120,\ 1/60,\ 1/30$. Fig. 16 compares the peak wall temperature distributions, in which $\bar{\Delta} = 0$ means the smooth tube and its bottom wall temperatures

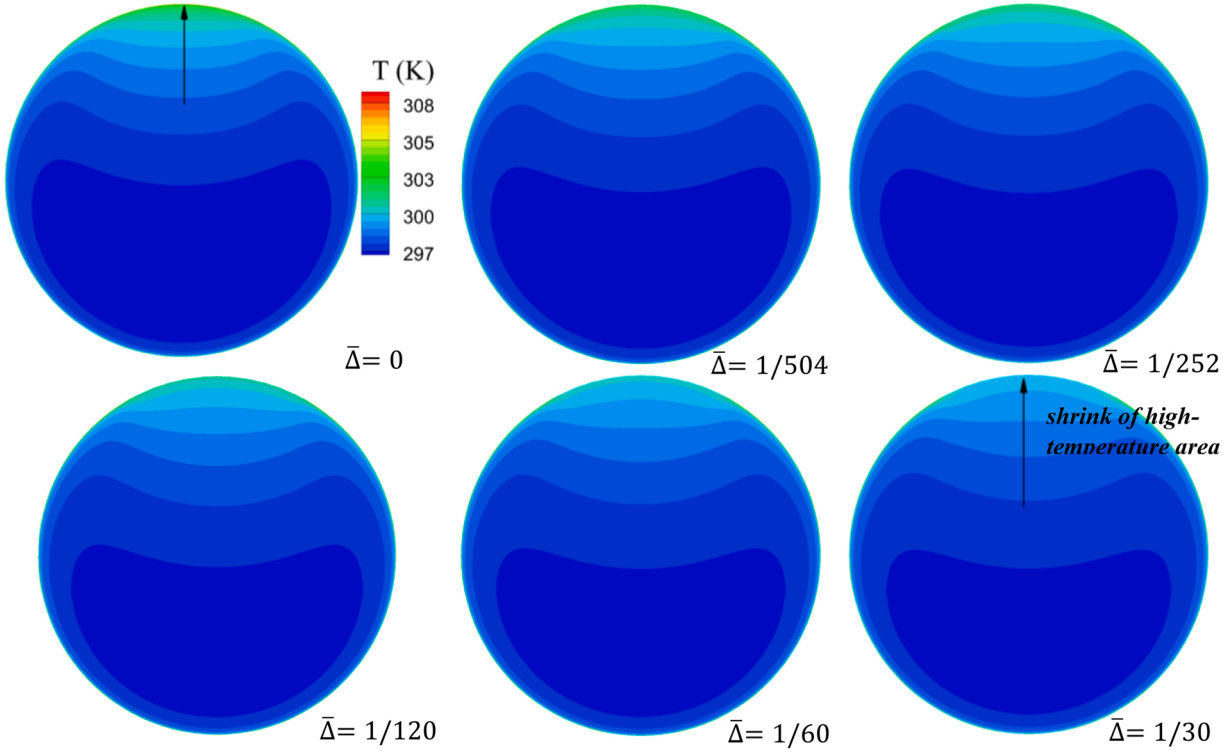

Fig. 17. Temperature contours of turbulent sCO_2 flows over cross section at $x_h/d = 150$ of partially ($\Phi_r = 60^\circ$) roughen horizontal tube with various roughness heights.

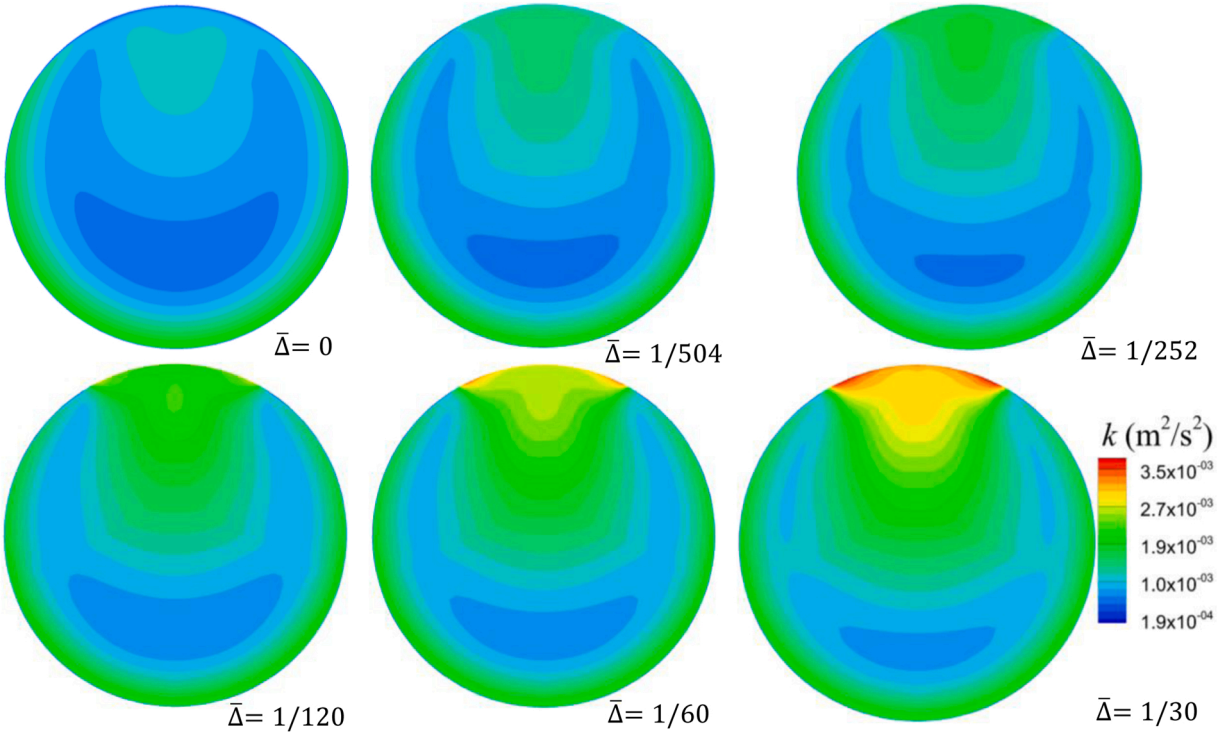

Fig. 18. Turbulence kinetic energy contours of sCO_2 flows over cross section at $x_h/d = 150$ of partially ($\Phi_r = 60°$) roughen horizontal tube with various roughness heights.

are also added as a representative to demonstrate the wall temperature non-uniformity. As seen, for the lower roughness heights, the top wall temperatures can be reduced. Still notably different to those of the bottom wall, as the roughness height increases, a more uniform wall temperature emerges. When the $\bar{\Delta}$ value reaches $1/120$, the temperature mismatch is reduced and the variation is negligible with further increase in the roughness. The top wall temperatures with $\bar{\Delta} = 1/60$ and $1/30$ nearly equal those of the bottom wall. An important comparison here is the one between the height of the roughness element and the boundary layer thickness. If roughness elements are tall enough to completely destroy the boundary layer, then any further increase in the height is unlikely to bring about tangible enhancements in heat transfer.

Figs. 17 and 18 display the temperature and the turbulence kinetic energy distributions, respectively, for a range of roughness heights. Here, the cross section at $x_h/d = 150$ is monitored where the difference in the wall temperature distributions is evident, as exhibited in Fig. 16. With the roughness implemented, the boundary layer is disturbed and with the rising roughness height the boundary layer can completely disappear. As seen, the turbulence kinetic energy production recovers near the top surface and increases with roughness heights, thereby heat transfer rate to sCO_2 increases and the high-temperature region around the top wall shrinks in size.

4. Conclusions

In order to mitigate the heat transfer deterioration commonly encountered along the top wall of horizontal supercritical piping flows then to improve the heat transfer uniformity over the circular perimeter, this paper introduces the simple and practical sand-grain roughness onto the tube surface and innovatively proposes the techniques of partially-roughen walls targeting more specifically on the degradation area. Based on the RANS simulations on the turbulent sCO_2 flows heating in a large horizontal pipe, the following conclusions can be drawn:

- The SST $k-\omega$ turbulence model exhibits the ability to give acceptable predictions on the sCO_2 heat transfer deterioration in the horizontal smooth tube and the pressure drop & heat transfer behaviors of rough piping flows.
- The uniform sand-grain roughness is quite practical and able to effectively alleviate the sCO_2 heat transfer impairment around the top wall caused by the buoyancy effects, the heat transfer homogeneity over the circumference is greatly improved, and the overall heat transfer performance is positively affected as well. These improvements are mainly attributed to that the incorporated roughness destroys the boundary (especially the viscous sublayer) and helps break the accumulation of hotter and lighter sCO_2 fluids near the top surface, which mitigates the blockage of the secondary circulation and recovers the turbulence activities in the top part. Also, the introduced roughness itself generates the vortexes that intensify the turbulence kinetic energy production near the wall as well.
- Even though the fully-roughened method can notably reduce the wall temperatures and enhance the sCO_2 heat transfer performance, the circumferential difference in heat transfer still exists or even grows over the entire perimeter and the friction loss is significant. The regional roughness approach targets more at the top deteriorated regime, particularly improves heat transfer near the top wall and achieves better uniformity over the circumference with remarkably less pressure drop. The optimal roughness proportion to gain the homogenous heat transfer with less friction loss can be closely dependent on the high-temperature regime caused by the accumulation.
- The roughness height has a significant influence. Due to the fact that the boundary layer which the roughness attempts to break possesses a certain thickness, as the roughness height is relatively low, the increasing roughness height is likely to bring more pronounced heat transfer improvements. While the roughness height goes up to certain high-level values ($1/120\,d$ under the studied conditions

involved in this work), its further increase generates slight difference.

Declaration of Competing Interest

The authors declare that they have no known competing financial interests or personal relationships that could have appeared to influence the work reported in this paper.

Data availability

Data will be made available on request.

Acknowledgments

This work is funded by National Natural Science Foundation of China through Grant number 52006248, and supported by Shenzhen Science and Technology Program (Grant No. RCBS20210706092408013) and the research start-up fund of the Recruited Hundred Talent Program equipped by Sun Yat-sen University (No. 76200-18841290).

References

[1] S. Duniam, I. Jahn, K. Hooman, Y. Lu, A. Veeraragavan, Comparison of direct and indirect natural draft dry cooling tower cooling of the sCO$_2$ Brayton cycle for concentrated solar power plants, Appl. Therm. Eng. 130 (2018) 1070–1080, https://doi.org/10.1016/j.applthermaleng.2017.10.169.

[2] P. Garg, P. Kumar, K. Srinivasan, Supercritical carbon dioxide Brayton cycle for concentrated solar power, J. Supercrit. Fluids 76 (2013) 54–60, https://doi.org/10.1016/j.supflu.2013.01.010.

[3] L. Hu, D. Chen, Y. Huang, L. Li, Y. Cao, D. Yuan, J. Wang, L. Pan, Investigation on the performance of the supercritical Brayton cycle with CO$_2$-based binary mixture as working fluid for an energy transportation system of a nuclear reactor, Energy 89 (2015) 874–886, https://doi.org/10.1016/j.energy.2015.06.029.

[4] P. Wu, Y. Ma, C. Gao, W. Liu, J. Shan, Y. Huang, J. Wang, D. Zhang, X. Ran, A review of research and development of supercritical carbon dioxide Brayton cycle technology in nuclear engineering applications, Nucl. Eng. Des. 368 (2020), 110767, https://doi.org/10.1016/j.nucengdes.2020.110767.

[5] M. Thirugnanasambandam, S. Iniyan, R. Goic, A review of solar thermal technologies, Renew. Sustain. Energy Rev. 14 (2010) 312–322, https://doi.org/10.1016/j.rser.2009.07.014.

[6] J.-F. Zhang, Y. Qin, C.-C. Wang, Review on CO$_2$ heat pump water heater for residential use in Japan, Renew. Sustain. Energy Rev. 50 (2015) 1383–1391, https://doi.org/10.1016/j.rser.2015.05.083.

[7] Y.-Y. Bae, H.-Y. Kim, D.-J. Kang, Forced and mixed convection heat transfer to supercritical CO$_2$ vertically flowing in a uniformly-heated circular tube, Exp. Ther. Fluid Sci. 34 (2010) 1295–1308, https://doi.org/10.1016/j.expthermflusci.2010.06.001.

[8] P.-X. Jiang, C.-R. Zhao, R.-F. Shi, Y. Chen, W. Ambrosini, Experimental and numerical study of convection heat transfer of CO$_2$ at super-critical pressures during cooling in small vertical tube, Int. J. Heat Mass Transf. 52 (2009) 4748–4756, https://doi.org/10.1016/j.ijheatmasstransfer.2009.06.014.

[9] Q. Zhang, H. Li, X. Kong, J. Liu, X. Lei, Special heat transfer characteristics of supercritical CO$_2$ flowing in a vertically-upward tube with low mass flux, Int. J. Heat Mass Transf. 122 (2018) 469–482, https://doi.org/10.1016/j.ijheatmasstransfer.2018.01.112.

[10] S. He, P.-X. Jiang, Y.-J. Xu, R.-F. Shi, W. Kim, J. Jackson, A computational study of convection heat transfer to CO$_2$ at supercritical pressures in a vertical mini tube, Int. J. Therm. Sci. 44 (2005) 521–530, https://doi.org/10.1016/j.ijthermalsci.2004.11.003.

[11] M. Sharabi, W. Ambrosini, Discussion of heat transfer phenomena in fluids at supercritical pressure with the aid of CFD models, Ann. Nucl. Energy 36 (2009) 60–71, https://doi.org/10.1016/j.anucene.2008.10.006.

[12] C.-R. Zhao, Z. Zhang, P.-X. Jiang, H.-L. Bo, Influence of various aspects of low Reynolds number k-ε turbulence models on predicting in-tube buoyancy affected heat transfer to supercritical pressure fluids, Nucl. Eng. Des. 313 (2017) 401–413, https://doi.org/10.1016/j.nucengdes.2016.12.033.

[13] J. Licht, M. Anderson, M. Corradini, Heat transfer and fluid flow characteristics in supercritical pressure water, J. Heat Transf. 131 (2009), https://doi.org/10.1115/1.3090817.

[14] J. Licht, M. Anderson, M. Corradini, Heat transfer to water at supercritical pressures in a circular and square annular flow geometry, Int. J. Heat Fluid Flow 29 (2008) 156–166, https://doi.org/10.1016/j.ijheatfluidflow.2007.09.007.

[15] P. Sassi, J. Pallarès, Y. Stiriba, Visualization and measurement of two-phase flows in horizontal pipelines, Exp. Comput. Multiph. Flow. 2 (2020) 41–51, https://doi.org/10.1007/s42757-019-0022-1.

[16] K. Tanimizu, R. Sadr, Experimental investigation of buoyancy effects on convection heat transfer of supercritical CO$_2$ flow in a horizontal tube, Heat Mass Transf. 52 (2016) 713–726, https://doi.org/10.1007/s00231-015-1580-9.

[17] T.H. Kim, J.G. Kwon, M.H. Kim, H.S. Park, Experimental investigation on validity of buoyancy parameters to heat transfer of CO$_2$ at supercritical pressures in a horizontal tube, Exp. Ther. Fluid Sci. 92 (2018) 222–230, https://doi.org/10.1016/j.expthermflusci.2017.11.024.

[18] Z. Liu, Q. Bi, Y. Guo, J. Yan, Z. Yang, Convective heat transfer and pressure drop characteristics of near-critical-pressure hydrocarbon fuel in a minichannel, Appl. Therm. Eng. 51 (2013) 1047–1054, https://doi.org/10.1016/j.applthermaleng.2012.10.029.

[19] Z. Yang, Q. Bi, Z. Liu, Y. Guo, J. Yan, Heat transfer to supercritical pressure hydrocarbons flowing in a horizontal short tube, Exp. Ther. Fluid Sci. 61 (2015) 144–152, https://doi.org/10.1016/j.expthermflusci.2014.10.024.

[20] G. Adebiyi, W. Hall, Experimental investigation of heat transfer to supercritical pressure carbon dioxide in a horizontal pipe, Int. J. Heat Mass Transf. 19 (1976) 715–720, https://doi.org/10.1016/0017-9310(76)90123-X.

[21] X. Chu, E. Laurien, Flow stratification of supercritical CO$_2$ in a heated horizontal pipe, J. Supercrit. Fluids 116 (2016) 172–189, https://doi.org/10.1016/j.supflu.2016.05.003.

[22] P. Forooghi, K. Hooman, Numerical study of turbulent convection in inclined pipes with significant buoyancy influence, Int. J. Heat Mass Transf. 61 (2013) 310–322, https://doi.org/10.1016/j.ijheatmasstransfer.2013.02.014.

[23] C. Eze, S.A. Khan, T. Lau, S. Ahmad, J. Zhao, Numerical study on the heat transfer deterioration and its mitigations for supercritical CO$_2$ flowing in a horizontal miniature tube, Ann. Nucl. Energy 151 (2021), 107982, https://doi.org/10.1016/j.anucene.2020.107982.

[24] J. Wang, Z. Guan, H. Gurgenci, K. Hooman, A. Veeraragavan, X. Kang, Computational investigations of heat transfer to supercritical CO$_2$ in a large horizontal tube, Energy Convers. Manag. 157 (2018) 536–548, https://doi.org/10.1016/j.enconman.2017.12.046.

[25] J. Wang, K. Qin, J. Gong, K. Hooman, Turbulent heat transfer of highly buoyant supercritical CO$_2$ flow in various horizontal pipes, Int. Commun. Heat Mass Transf. 133 (2022), 105939, https://doi.org/10.1016/j.icheatmasstransfer.2022.105939.

[26] Y.Y. Bae, H.Y. Kim, T.H. Yoo, Effect of a helical wire on mixed convection heat transfer to carbon dioxide in a vertical circular tube at supercritical pressures, Int. J. Heat Fluid Flow. 32 (2011) 340–351, https://doi.org/10.1016/j.ijheatfluidflow.2010.06.013.

[27] Z. Li, G. Tang, Y. Wu, Y. Zhai, J. Xu, H. Wang, J. Lu, Improved gas heaters for supercritical CO$_2$ Rankine cycles: Considerations on forced and mixed convection heat transfer enhancement, Appl. Energy 178 (2016) 126–141, https://doi.org/10.1016/j.apenergy.2016.06.018.

[28] Z. Li, J. Lu, G. Tang, Q. Liu, Y. Wu, Effects of rib geometries and property variations on heat transfer to supercritical water in internally ribbed tubes, Appl. Therm. Eng. 78 (2015) 303–314, https://doi.org/10.1016/j.applthermaleng.2014.12.067.

[29] Z. Li, Y. Wu, G. Tang, J. Lu, H. Wang, Numerical analysis of buoyancy effect and heat transfer enhancement in flow of supercritical water through internally ribbed tubes, Appl. Therm. Eng. 98 (2016) 1080–1090, https://doi.org/10.1016/j.applthermaleng.2016.01.007.

[30] Z.B. Liu, Y.L. He, Y.S. Li, Z.G. Qu, W.Q. Tao, Heat transfer characteristics of supercritical CO$_2$ flow in metal foam tubes, J. Supercrit. Fluids 101 (2015) 36–47, https://doi.org/10.1016/j.supflu.2015.03.002.

[31] Z.B. Liu, Y.L. He, Z.G. Qu, W.Q. Tao, Experimental study of heat transfer and pressure drop of supercritical CO$_2$ cooled in metal foam tubes, Int. J. Heat Mass Transf. 85 (2015) 679–693, https://doi.org/10.1016/j.ijheatmasstransfer.2015.02.013.

[32] Z. Li, Y. Yao, Q. Wang, J. Cai, Y. Wu, H. Wang, Effect of internal helical-rib roughness on mixed convection flow and heat transfer in heated horizontal pipe flow of supercritical water, Int. J. Heat Mass Transf. 130 (2019) 1272–1287, https://doi.org/10.1016/j.ijheatmasstransfer.2018.11.045.

[33] A. Lock, K. Hooman, Z. Guan, A detailed model of direct dry-cooling for the supercritical carbon dioxide Brayton power cycle, Appl. Therm. Eng. 163 (2019), 114390, https://doi.org/10.1016/j.applthermaleng.2019.114390.

[34] P. Forooghi, M. Stripf, B. Frohnapfel, A systematic study of turbulent heat transfer over rough walls, Int. J. Heat Mass Transf. 127 (2018) 1157–1168, https://doi.org/10.1016/j.ijheatmasstransfer.2018.08.013.

[35] P. Orlandi, D. Sassun, S. Leonardi, DNS of conjugate heat transfer in presence of rough surfaces, Int. J. Heat Mass Transf. 100 (2016) 250–266, https://doi.org/10.1016/j.ijheatmasstransfer.2016.04.035.

[36] R. Olmeda, A. Doehring, C. Stemmer, Study and application of wall-roughness models in LES flows, Int. J. Heat Fluid Flow. 95 (2022), 108948, https://doi.org/10.1016/j.ijheatfluidflow.2022.108948.

[37] S. Zhang, X. Xu, C. Liu, C. Dang, A review on application and heat transfer enhancement of supercritical CO$_2$ in low-grade heat conversion, Appl. Energy 269 (2020), 114962, https://doi.org/10.1016/j.apenergy.2020.114962.

[38] F.R. Menter, Two-equation eddy-viscosity turbulence models for engineering applications, AIAA J. 32 (1994) 1598–1605, https://doi.org/10.2514/3.12149.

[39] A. Tikadar, U. Najeeb, T.C. Paul, S.K. Oudah, A.S. Salman, A.M. Abir, L.A. Carrilho, J.A. Khan, Numerical investigation of heat transfer and pressure drop in nuclear fuel rod with three-dimensional surface roughness, Int. J. Heat Mass Transf. 126 (2018) 493–507, https://doi.org/10.1016/j.ijheatmasstransfer.2018.05.141.

[40] X. Liu, X. Xu, C. Liu, J. Ye, H. Li, W. Bai, C. Dang, Numerical study of the effect of buoyancy force and centrifugal force on heat transfer characteristics of supercritical CO$_2$ in helically coiled tube at various inclination angles, Appl. Therm. Eng. 116 (2017) 500–515, https://doi.org/10.1016/j.applthermaleng.2017.01.103.

[41] S. Zhang, X. Xu, C. Liu, X. Liu, Z. Ru, C. Dang, Experimental and numerical comparison of the heat transfer behaviors and buoyancy effects of supercritical

CO_2 in various heating tubes, Int. J. Heat Mass Transf. 149 (2020), 119074, https://doi.org/10.1016/j.ijheatmasstransfer.2019.119074.
[42] M. Xiang, J. Guo, X. Huai, X. Cui, Thermal analysis of supercritical pressure CO_2 in horizontal tubes under cooling condition, J. Supercrit. Fluids 130 (2017) 389–398, https://doi.org/10.1016/j.supflu.2017.04.009.
[43] J. Guo, M. Xiang, H. Zhang, X. Huai, K. Cheng, X. Cui, Thermal-hydraulic characteristics of supercritical pressure CO_2 in vertical tubes under cooling and heating conditions, Energy 170 (2019) 1067–1081, https://doi.org/10.1016/j.energy.2018.12.177.
[44] Z. Li, Y. Wu, G. Tang, D. Zhang, J. Lu, Comparison between heat transfer to supercritical water in a smooth tube and in an internally ribbed tube, Int. J. Heat Mass Transf. 84 (2015) 529–541, https://doi.org/10.1016/j.ijheatmasstransfer.2015.01.047.
[45] J. Nikuradse, Laws of flow in rough pipes, J. Appl. Phys. 3 (1950).